Journal of Power Sources 400 (2018) 284–295

Contents lists available at ScienceDirect

Journal of Power Sources

journal homepage: www.elsevier.com/locate/jpowsour

Modeling liquid water re-distributions in bi-porous layer flow-fields of proton exchange membrane fuel cells

Jinyong Kim[a], Gang Luo[b], Chao-Yang Wang[a,*]

[a] Electrochemical Engine Center (ECEC), Department of Mechanical & Nuclear Engineering, The Pennsylvania State University, University Park, PA, 16802, USA
[b] EC Power, 341 Science Park Road, State College, PA, 16803, USA

HIGHLIGHTS

- A bi-porous layer flow-field has a secondary porous layer attached to a BP.
- Secondary porous layers cause liquid water re-distribution inside flow-fields.
- Liquid water re-distribution enhances water management and mass transport.
- Flooding occurs if the permeability ratio exceeds a threshold.
- Flooding in secondary porous layers results in poor cell performance.

ARTICLE INFO

Keywords:
Liquid water management
Bi-porous layer flow-fields
Capillary force
High current density
Liquid water re-distribution
PEMFC

ABSTRACT

A bi-porous layer flow-field features a secondary porous layer of smaller permeability attached to a bi-polar plate to remove excessive liquid water from the main flow-field by capillary-induced liquid water re-distributions, therefore enhances liquid water management of a proton exchange membrane fuel cell (PEMFC). In this work, we present a two-dimensional two-phase model to elucidate the underlying physics of liquid water re-distribution inside a bi-porous layer flow-field. We reveal that liquid water re-distribution can improve liquid water management in the flow-field and gas diffusion layer, leading up to significant enhancement in oxygen diffusion to the catalyst layer. However, if permeability of the secondary porous layer is too low and the permeability ratio exceeds a threshold, the secondary porous layer may suffer from flooding. This causes liquid water build-up in the main flow-field and GDL, which leads poor oxygen diffusion to the catalyst layer and hence operational instability. The threshold permeability ratio is analytically derived, and flow behaviors at conditions above and below the threshold permeability ratio are explored numerically and analytically. We suggest choosing a permeability ratio below the threshold permeability ratio to avoid flooding in the secondary porous layer and to fully utilize the benefits of liquid water re-distributions.

1. Introduction

Improper management of liquid water in flow-fields and adjacent gas diffusion layers (GDLs) causes detrimental loss in durability and performance of proton exchange membrane fuel cells (PEMFCs), especially for automotive applications of PEMFCs due to high current density operation. First, liquid water accumulation in flow-fields results in higher liquid water saturation in GDLs, which causes oxygen starvation in catalyst layers (CL) and greatly increases mass transport losses. Second, liquid water droplets in flow-fields block pathways for reactant gas and therefore cause cell voltage oscillations and even shut-down reactant gas flow [1], which decreases cell's active area and also causes detrimental consequences to cell durability [2]. A novel approach for effectively removing excessive liquid water in flow-fields of PEMFCs is in urgent need for improving performance and stability of PEMFC.

One way to enhance liquid water management in PEMFC flow-fields is using a capillary force to re-distribute liquid water inside flow-fields. For example, as schematically shown in Fig. 1a, one can attach a secondary porous layer of lower permeability to a bi-polar plate to absorb excessive liquid water from the main flow-field by using the capillary force, like a sponge absorbing liquid water. Subsequently, this liquid water imbibed inside the finer porous layer is forced to move toward the outlet under the longitudinal pressure drop created by reactant gas flowing in adjacent main flow-field. This “liquid water re-distribution”

* Corresponding author.
E-mail address: cxw31@psu.edu (C.-Y. Wang).

https://doi.org/10.1016/j.jpowsour.2018.08.018
Received 1 March 2018; Received in revised form 17 April 2018; Accepted 7 August 2018

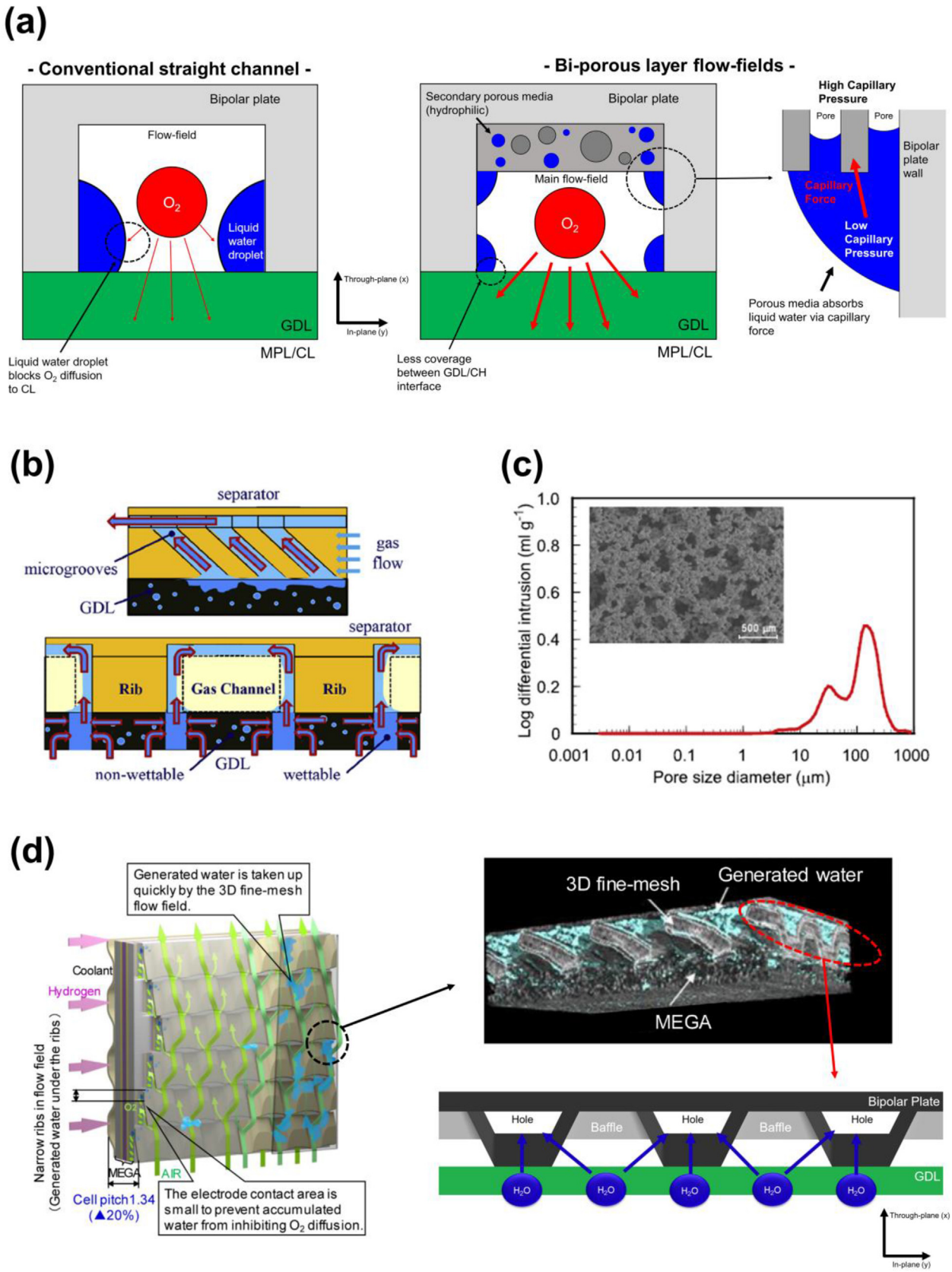

Fig. 1. (a) Schematics and working principles of bi-porous layer flow-fields, **(b–d)** Examples of flow-fields utilizing liquid water re-distribution: **(b)** micro-grooved flow-fields [7] **(c)** bi-porous flow-fields [8] **(d)** 3D fine-mesh flow-fields of Toyota Mirai (macro flow-fields [9] and CT image [9]).

in such flow-fields enhances oxygen diffusion to CL by reducing liquid water coverage between flow-fields and GDL [3]. This also improves fuel cell operational stability by decreasing amount of liquid water in main flow-fields, which is the main cause of pressure and voltage fluctuations [4]. Considering that flow channel itself also can be considered as a porous medium [4], this flow-field is termed as "bi-porous layer (or bi-layer) flow-field" in this study.

So far, three different types of flow-fields (Fig. 1b–d) in prior experimental studies have shown strong resemblance to bi-porous layer flow-fields, as they all use capillary force to trigger liquid water re-distribution. The first example is a micro-grooved flow-field (Fig. 1b) [5–7], which is first developed by Utaka et al. [5]. As shown in Fig. 1b, micro-grooves captivate liquid water inside the flow-field by capillary force and remove liquid water through the outlet via gas shear stress [5–7]. Improvements in cell current density and power density by 16.1% and 3.2%, respectively, were reported by Koresawa and Utaka [6]. Furthermore, Utaka and Koresawa [7] showed that current and power density can be maximized by increasing capillary forces with stronger hydrophilic treatment (contact angle = 20°).

The second example is a bi-porous flow-field (Fig. 1c), which has two characteristic pore diameters in the porous flow-field [8]. Kozacai et al. [8] first manufactured a hydrophilic bi-porous flow-field, in order to prevent water flooding in the flow-field and improve reactant gas diffusion by relocating liquid water from large pores to smaller pores by capillary force. Kozacai et al. [8] reported that bi-porous flow-fields are advantageous over mono-porous flow-fields, especially under high current density operation.

The last example is 3D fine-mesh flow-fields of Toyota Mirai (Fig. 1d) [9–11]. As shown in Fig. 1d, small holes drilled into the bi-polar plate drain liquid water from the main flow-field by capillary force [9]. Therefore, much more liquid water appears at upper bi-polar plate side as clearly seen in CT image [9], rather than interface between the main flow-field and GDL [9]. This liquid water re-distribution mechanism, along with Forchheimer's inertial effect [12], has significantly improved liquid water management as well as mass transport of Toyota Mirai fuel cell stack, resulting in 2.4 time increase of limiting current density compared to their earlier model [10,11].

The examples cited above have established the benefits of liquid water re-distribution in terms of liquid water management. However, the theoretical elucidation of liquid water re-distribution has been absent in the literature. To fully utilize the advantages of liquid water re-distribution, understanding physical mechanisms of liquid water re-distribution as well as quantifying key parameters, such as amount of liquid water and liquid water velocity, are crucial to PEMFC design.

In this work, we target the bi-porous layer flow-field to study underlying physics of liquid water re-distribution in PEMFCs, since it is the simplest type of flow-fields among above mentioned flow-fields and therefore best candidate to address the physics. We use a macroscopic two-dimensional (2D) two-phase flow model based on multi-phase mixture (M^2) formulation [13,14]. We first quantify liquid water saturations as well as velocity distributions of each phase with 2D simulation under various permeability ratio. We then elucidate the underlying physics that causes the liquid water re-distribution between the two layers and driving forces that remove the liquid water in the secondary porous layer through the outlet. Finally, we discuss the effect of liquid water re-distributions in bi-porous layer flow-fields on fuel cell performance.

2. Numerical model

2.1. Model assumptions

A simple 2D model is used to demonstrate underlying physics and the effect of liquid water re-distribution in bi-porous layer flow-fields on PEMFC performance. The computational domain in current work is restricted to cathode side since water flooding in cathode is more important than anode due to sluggish oxygen reduction reaction (ORR). Then, following assumptions are made for the simplifications.

- Steady, isothermal (no source term due to condensation/evaporation)
- Uniform current density at GDL/CL interface
- Fully humidified condition (whole domain is two-phase region)
- Forchheimer's inertial effect is neglected due to fully-developed flow in flow-fields
- Negligible gravity effect.

2.2. Governing equations

We treat main flow-fields as 2D straight channels. Following the approach by Wang et al. [4], the 2D straight channels are treated as structured and ordered porous media, while this analysis also can be applied if actual porous flow-fields are used for main flow-fields. Therefore, whole computational domain is treated as porous media. The multi-phase mixture (M^2) model, which describes two-phase flow in porous media [13,14], is then selected as a two-phase model. Based on the assumptions made earlier, governing equations based on M^2 formulation [13,14] are simplified and shown as follows:

Continuity equation:

$$\nabla\cdot(\rho\vec{u}) = 0 \tag{1}$$

Momentum conservation equation:

$$\nabla P = -\frac{\mu}{K}\vec{u} \tag{2}$$

Species conservation equation:

$$\nabla\cdot(\gamma_c\vec{u}C_i) = \nabla\cdot(D_{i,g}^{eff}\nabla C_i) - \nabla\cdot\left(\left(\frac{mf_l^i}{MW^i} - \frac{C_{i,g}}{\rho_g}\right)\vec{j}_l\right) + \dot{S}_i \tag{3}$$

where capillary diffusion flux, $\vec{j}_l$, is expressed as

$$\vec{j}_l = \frac{K\lambda(1-\lambda)}{\nu}\nabla P_c \tag{4}$$

The details of all physical parameters, constitutive relationships and parameters of Eqs. (1)–(5) are not repeated here since they can be found in Ref. [15].

The intrinsic permeability of flow-fields can be evaluated by Hagen-Poiseuille equation:

$$K = c\frac{D_h^2}{32} \tag{5}$$

where D_h is a hydraulic diameter and c is a shape factor. 2D straight channel flow-fields are equivalent to flow-fields between two parallel plates. Therefore, the shape factor, c, is 2/3 [16] and the hydraulic diameter is twice of the channel height, which are used to evaluate a permeability of main flow-fields (K_1). For three-dimensional flow-fields of PEMFCs, readers can refer to shape factors and hydraulic diameters of different cross-sectional geometry in Ref. [17]. Also, it should be noted that shape factors and hydraulic diameters may also be affected by the pressure exerted on MEA, causing GDL intrusion in flow-fields and decreased permeability of flow-fields [18]. For secondary porous layers, different permeabilities are prescribed depending on various permeability ratios ($K_1/K_2 = R_K$) to study the effect of permeability of secondary porous layers on two-phase flow behavior.

Capillary pressure, P_c, can be described as

$$P_c = \frac{\sigma\cos\theta_w J(s_w)}{\sqrt{K/\varepsilon}} \tag{6}$$

where $J(s_w)$ is a Leverett-J function. In this work, we choose Brook-Corey type Leverett-J function [19–24] as:

$$J(s_w) = \begin{cases} J_c \times s_w^{(-1/\lambda_{BC})} & \text{for } 0 \le s_w < 1 \\ 0 < J(s_w) \le J_c & \text{for } s_w = 1 \end{cases} \quad (7)$$

where J_c and λ_{BC} are the fitting parameter of Brook-Corey model, which are determined by pore size distributions and structures of porous media [19–24]. Typical capillary pressure curves based on Brook-Corey model are shown in Fig. 5a. As it can be seen from Eq. (7) and Fig. 5a, the capillary pressure decreases as the wetting fluid saturation increases due to the increasing droplet size of wetting fluid. However, if the capillary pressure reaches entry pressure ($P_e = \sigma \cos\theta J_c/(\sqrt{K/\varepsilon})$) as wetting fluid saturation reaches to 1, solid surfaces are completely wetted by the wetting fluid and capillary pressure can range between P_e and 0 [19–24]. Readers interested in the detailed physical background of Brook-Corey model may refer to Ref. [24]. In the present work, $J_c = 0.6274$ and $\lambda_{BC} = 2.528$ are used as from Gostick et al. [20], which measured relationship between $J(s_w)$ and saturation (s_w) of 8 different kinds of commercially available GDLs and found that this $J(s_w) - s_w$ relationship can be reasonably collapsed into single curve, with either Brook-Corey [24] or van Genuchten [25] type function. Since it is likely that the characteristic pore size of secondary porous layers (~10–100 μm) is between the pore size of GDLs (10 μm) and that of flow-fields (~100 μm), using the parameters from Gostick et al. [20] can be a good approximation. For hydrophilic media (i.e. hydrophilic flow-fields), wetting-phase saturation (s_w) is liquid water saturation (s), while s_w is gas saturation ($1 - s$) for hydrophobic material (i. e. GDL).

Effective oxygen diffusivity can be described by Bruggeman correlations:

$$D_{O_2}^{eff} = \varepsilon^m (1 - s)^n D_{O_2} \quad (8)$$

where Bruggeman factor $m = n = 3.0$ is used followed by Wang and Wang [26]. Basu et al. [27] showed that the capillary diffusion term in oxygen conservation equation (Eq. (3)) is small compared to molecular diffusion term or convection term. Therefore, the second term in RHS of oxygen conservation equation (oxygen transport due to capillary diffusion) is neglected in the numerical implementation. The oxygen diffusion coefficient, D_{O_2}, is obtained from the expression by Bird et al. [28].

2.3. Computational geometry and boundary conditions

Detailed computational geometry and boundaries are shown in Fig. 2. Common 20 cm-long flow-fields with 4000 hexagonal cells are used for a straight channel. Roughly five times larger number of cells along flow-direction, with the total number of 20,800, are used for bi-porous layer flow-fields, since the saturation variation along flow direction (z) in the cases with bi-porous layer flow-fields are much larger (0–1), than the cases with a straight channel (0–0.2). The straight channel case serves as a baseline, in order to compare bi-porous layer flow-fields with conventional flow-fields. Inlet oxygen mole fraction is set to be 0.21 and inlet velocity boundary condition is applied as:

$$\overrightarrow{u_{in}} = \xi_{O_2} \frac{I}{4FC_{O_2}} \frac{A_{mem}}{A_{inlet}} \quad (9)$$

where ξ_{O_2} is an oxygen stoichiometry ratio and I is a current density. At solid walls, impermeable conditions for flow and zero-gradient conditions for other scalars are applied.

At GDL/CL interface, liquid and oxygen flux can be described as follows and set as boundary conditions.

$$\dot{n}'_{H_2O} = \frac{I(1 + 2\alpha)}{2F} \quad (10)$$

$$\dot{n}'_{O_2} = \frac{I}{4F} \quad (11)$$

where α in Eq. (15) is a net water transport coefficient due to water back-diffusion and electro-osmotic drag, which is usually in the range between −0.4 and 0.4, according to Liu et al. [26]. In this work, we consider a case with zero net water transport coefficient, while analysis with non-zero α is also possible with the current numerical model.

2.4. Operating conditions and numerical methods

Physical and geometrical parameters used in this work are listed in Table 1. And operating conditions are listed in Table 2. All governing equations are discretized and solved by using a commercial CFD software, Fluent® (version 15.0), with SIMPLE algorithm for pressure-velocity coupling [29]. User-defined scalars (UDS) are added to implement customized governing equations. Boundary conditions, transport properties and source terms then are applied and evaluated during calculations via user-defined functions (UDF). Species and liquid water imbalances less than 1% are achieved and considered as convergence criteria for all simulations. In this work, we selected the current density of 2.0 A cm^{-2} and air stoichiometry of 2.0, common operating conditions for automotive applications [30].

3. Results and discussion

This section is organized as follows. First, liquid saturation and velocity distributions for each phase are quantified and shown using the current model. Then, we answer the main physical mechanisms that causes liquid saturation re-distribution between the two layers numerically and analytically. Finally, we discuss the effects of liquid saturation re-distribution on cell performance by showing liquid water distributions in GDL and oxygen distributions in CL.

One may wonder how to select appropriate materials for secondary porous layers. The two major properties that characterize porous media are porosity and permeability. We expect that secondary porous layers are highly porous ($\varepsilon > 0.8$) and have similar volume to main flow-fields, to captivate large amount of water from main flow-fields. Therefore, permeability (K_2) is the most important property for secondary porous layers. Hence, the most important non-dimensional number is the permeability ratio ($R_K = K_1/K_2$). In this regard, liquid water re-distributions and related phenomena are described under various permeability ratios in this work.

3.1. Liquid saturation and phase velocity distributions

Fig. 3 shows liquid water saturation profiles at secondary porous layers and main flow-fields with various permeability ratios, along channel direction. First, liquid saturation profiles at secondary porous layers are shown in Fig. 3a. It can be found that liquid saturation curves at secondary porous layers increase with increasing permeability ratio, which can be compared to the real-life situation that finer sponge can absorb liquid water more effectively. In the case of $R_K = 100$, liquid saturation at outlet reaches 0.95, which indicates that the secondary porous layer is almost fully saturated.

However, as it can be seen in the cases of $R_K = 200$ and 500, increasing permeability ratio further results in flooding inside secondary porous layers. Starting from a flooding point (L_{fl}), where liquid water saturation first starts to reach 1.0, flow becomes single-phase of liquid ($s = 1.0$). It is also noteworthy that flooding region (single-phase) expands with increasing permeability ratio.

Fig. 3b presents liquid saturation profiles at main flow-fields. As seen in the figure, liquid saturation curves in main flow-fields decrease with increasing permeability ratio until $R_K = 100$ due to increasing liquid water absorption by secondary porous layers. It is interesting to note that the liquid water saturation in the case of $R_K = 10$ shows almost 10% of liquid water saturation compared to the straight channel case at outlet region, while this value is further decreased to 1% in the case of $R_K = 100$. This implies that adding a secondary porous layer can effectively decrease large amount of liquid water in a main flow-field.

However, increasing permeability ratio further causes liquid water

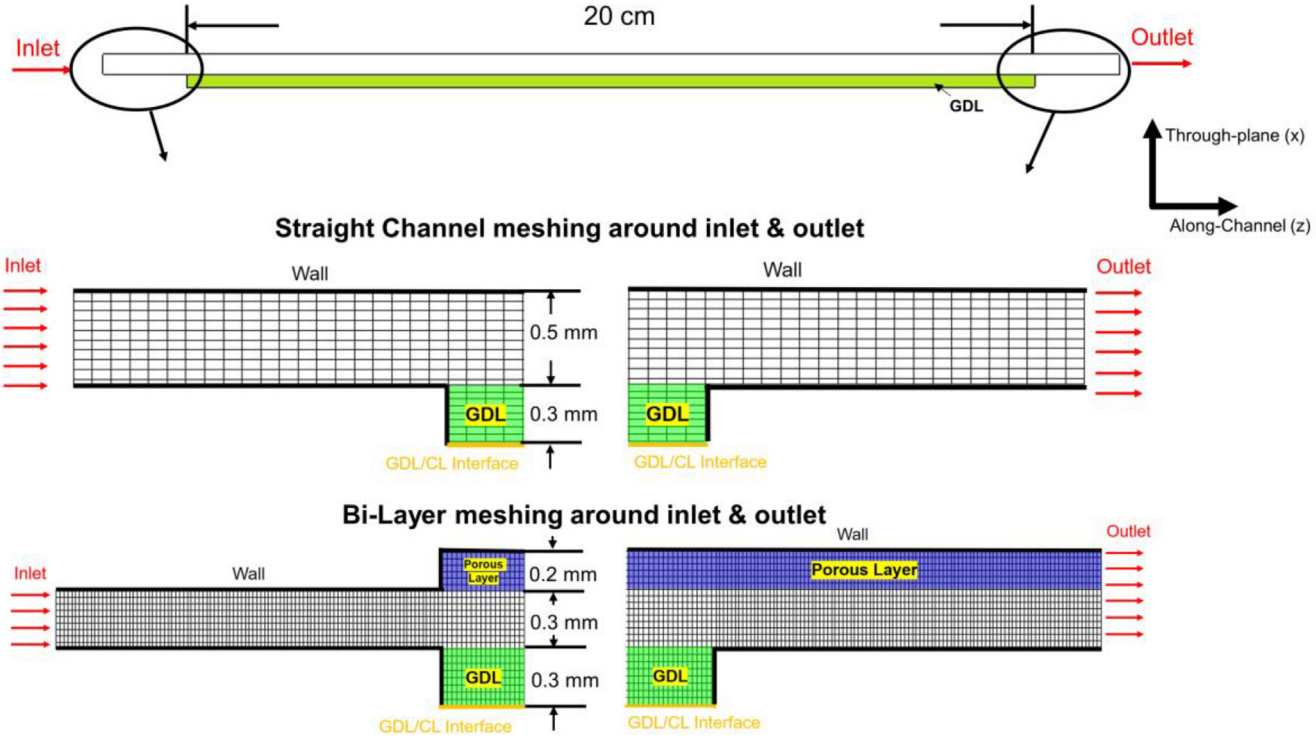

Fig. 2. Computational geometry and meshing of straight channel case and bi-porous layer case.

Table 1
Physical, geometrical parameters and operating conditions.

Parameters	Value
GDL thickness	300 μm
Contact angle of GDLs/flow-fields	110/70°
Porosity of secondary porous layers /GDLs	0.9/0.75
Permeability of GDLs	1.0×10^{-11}m^2
Permeability of main flow-fields (single channel/ bi-porous flow-fields)	$2.08 \times 10^{-8}/7.5 \times 10^{-9}$m^2
Bruggemann factor [26]	3.0
Oxygen diffusion coefficient [28]	1.44×10^{-5}m^2/s
Power factor in relative permeability (n_k) [4]	4.0 (for both gas and liquid)

Table 2
Operating conditions.

Parameters	Value
Inlet pressure	2.0 atm
Inlet temperature	55 °C
Inlet dew point	55 °C
Cathode stoichiometry	2.0
Current density	2.0 A cm^{-2}

accumulation in main flow-fields. In both cases (R_K = 200 and 500), liquid water starts to accumulate in main flow-fields from the flooding points since secondary porous layers become single phase of liquid and therefore cannot hold up more liquid from the flooding points. In the case of R_K = 500, the liquid water saturation at outlet even reaches even as high as 0.18.

Detailed liquid and gas velocity distributions near outlet region (170 mm < z < 180 mm) are shown in Fig. 4 to illustrate liquid and gas flow behavior in bi-porous flow-fields. Liquid and gas velocity are evaluated as [14]:

$$\vec{u_l} = \left(\rho\vec{u}\lambda + \frac{K\lambda(1-\lambda)}{\nu}\nabla P_c\right)/\rho_l \tag{12}$$

$$\vec{u_g} = (\rho\vec{u} - \rho_l\vec{u_l})/\rho_g \tag{13}$$

In Fig. 4, cases of R_K = 2, 100 and 500 are particularly selected and shown. Each case (R_K = 2, 100 and 500) represents following:

- R_K = 2: a case with coarse secondary porous layer
- R_K = 100: a case that most of liquid water in main flow-field is absorbed by secondary porous layer
- R_K = 500: a case with severe flooding in secondary porous layer

The baseline case (single straight channel case) is first shown in Fig. 4a–b. Compared to the baseline case, bi-layer cases show an interesting point that liquid velocities in secondary porous layer are considerably larger than those in main flow-fields, even in severe flooding case (R_K = 500). Consequently, gas velocities in secondary porous layer are significantly smaller than those in main flow-fields, even using a very coarse porous layer (R_K = 2). This suggests that bi-porous layer flow-fields can effectively separate liquid and gas flow. In other words, liquid water flows mainly along secondary porous layers while reactant gas mainly flows through main flow-fields, because of liquid re-distribution in bi-porous flow-fields.

More detailed liquid velocity distributions in region A (marked in Fig. 4c, e, g) are shown to investigate liquid water flow behavior in main flow-fields. Compared to the other cases, axial (along-channel direction (z)) liquid velocity is almost zero in the case of R_K = 100, since most of liquid water in main flow-fields is absorbed to secondary porous media along through-plane direction (see Fig. 3b). In a severe flooding case (R_K = 500), axial liquid velocity becomes dominant since large amount of liquid water should also move out through main flow-fields due to flooding in secondary porous layer.

3.2. Flow behavior at conditions below and above the threshold permeability ratio

In the previous section, we observed that adding a secondary porous layer into a flow-field leads significant liquid water saturation and liquid velocity differences between the two layers. Also, it is found that

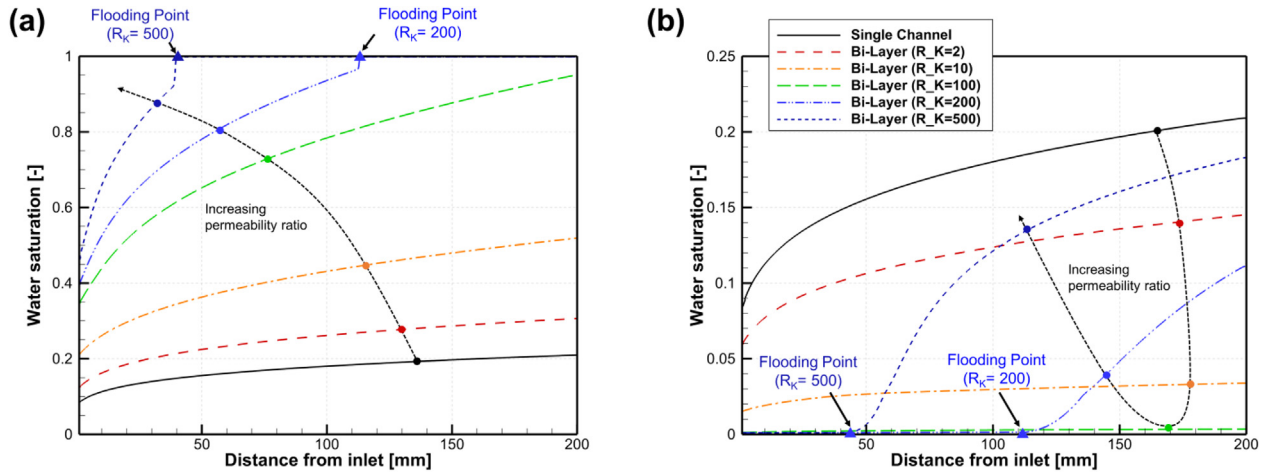

Fig. 3. Liquid saturation profile at (a) secondary porous layer (b) main flow-fields along channel directions.

flow behaviors in the cases of $R_K = 2$, 10 and 100 are fundamentally different from them in the cases of $R_K = 200$ and 500, which is mainly because of flooding in secondary porous layers. Therefore, the following questions arise:

1. What is the threshold value of permeability ratio ($R_{K,th}$) that determines transition between non-flooding ($s_2 < 1$) to flooding ($s_2 = 1$) in a secondary porous layer?
2. What are the main physics that governs flow behaviors at conditions below$R_{K,th}$ and above$R_{K,th}$?

In this section, we attempt to answer above questions. First, the threshold permeability ratio, $R_{K,th}$, is defined as a permeability ratio at which flooding in a secondary porous layer ($s_2 = 1$) starts to occur. To derive an expression for $R_{K,th}$, we first assume that liquid water transport along flow direction (z) is dominated by two-phase flow in the flow-field and secondary layer. In comparison, liquid water transport along flow direction (z) through GDL is negligible because of GDL's hydrophobicity, much smaller pore size (and hence smaller permeability) and smaller thickness than the secondary porous layer in the flow-field. Then, gas momentum equation for a main flow-field (Eq. (14)) and liquid momentum equation for a secondary porous layer (Eq. (15)) at outlet region along axial direction (z) are first shown below, since flooding first appears in a secondary porous layer at outlet region:

$$\frac{\partial P_g}{\partial z} = -\frac{\nu_g}{K_{g,1}}\rho_g u_{g,z} \tag{14}$$

$$\frac{\partial P_l}{\partial z} = -\frac{\nu_l}{K_{l,2}}\rho_l u_{l,z} \tag{15}$$

where K_l, K_g is a liquid-phase and a gas-phase permeability, respectively. Both can be expressed as $K_k = KK_{rk}$ where K_{rk} is a relative permeability of phase-k. The relative permeability of phase-k is often described by power-law such that $K_{rk} = s_k^{n_k}$[31]. At the threshold permeability ratio condition, the relative permeability of liquid in a secondary porous media is 1 at outlet, simply due to flooding ($s = 1$). Also, the relative permeability of gas in a main flow-field can be approximated to 1 at the threshold permeability ratio condition, since most of liquid water is absorbed to adjacent secondary porous layer (s = 0) due to high capillary force.

Assuming negligible pressure difference between gas and liquid ($P_g \sim P_l$) in x-direction due to small velocity in through-plane direction, axial pressure gradients for both phases are approximately equal ($\partial P_g/\partial z = \partial P_l/\partial z$). And considering that mass flow rate of each phase in each layer along the longitudinal direction can be expressed as $\dot{m}_k = \rho_k u_{k,z} A$, the ratio of the liquid mass flow rate through a secondary porous layer to the gas mass flow rate through a main flow-field can be expressed as:

$$\frac{\dot{m}_{l,2}}{\dot{m}_{g,1}} = \left(\frac{\nu_g A_2}{\nu_l A_1}\right)/(R_{K,th}) \tag{16}$$

Mass flow rate in a cathode channel remains relatively uniform since mass fraction of nitrogen is dominant in reactant gas. Therefore, the gas mass flow rate can be approximated as $\dot{m}_g = (\xi_{O_2} MW_{air} A_{mem} I)/(4FX_{O_2,in})$ according to Eq. (9), while total liquid water generation rate can be expressed as $\dot{m}_{l,tot} = (1+\alpha) \times (MW_{H_2O} A_{mem} I)/(2F)$ under fully humidified conditions. Therefore, Eq. (16) is re-arranged as:

$$\frac{\dot{m}_{l,2}}{\dot{m}_{l,tot}} = 0.8\left(\frac{\xi_{O_2}\nu_g A_2}{(1+\alpha)X_{O_2,in}\nu_l A_1}\right)/(R_{K,th}) \tag{17}$$

A similar expression for cases with partially humidified inlets is also derived and found in Appendix. LHS of Eq. (17) stands for the fraction of liquid water flow rate through a secondary porous layer, compared to total liquid water flow rate. At the threshold permeability ratio, LHS of Eq. (17) is 1 since most of liquid water from a main flow-field is absorbed by adjacent secondary porous layer. Then, the threshold permeability ratio can be expressed as:

$$R_{K,th} = 0.8\left(\frac{\xi_{O_2}\nu_g A_2}{(1+\alpha)X_{O_2,in}\nu_l A_1}\right) \tag{18}$$

The threshold permeability ratio increases with increasing gas velocity (low operating pressure, high stoichiometry) and decreasing relative humidity (see Appendix). Under the current simulation conditions, $R_{K,th}$ is found to be 150, which is between 100 and 200 as expected.

At conditions below$R_{K,th}$, liquid saturations in secondary porous layers are below 1.0 and the liquid water absorption from main flow-fields depends on capillary conditions. However, at conditions above $R_{K,th}$, partial regions in secondary porous layers become single-phase liquid, and therefore the liquid water absorption from main flow-fields is limited. In the following section, we elucidate flow behavior at conditions below and above the threshold permeability ratio analytically in detail.

3.2.1. Flow behavior at conditions below the threshold permeability ratio

First, we evaluate the time scale for a liquid droplet to travel from cathode inlet to outlet. Based on the liquid velocity profile ($10^{-3\sim-4}$m s^{-1}) in Fig. 4, it can be shown that this time scale is on the order of $10^{2\sim3}$sec considering the length scale of cathode channel is ~0.1 m, which is in consistent with prior experimental [32] and numerical

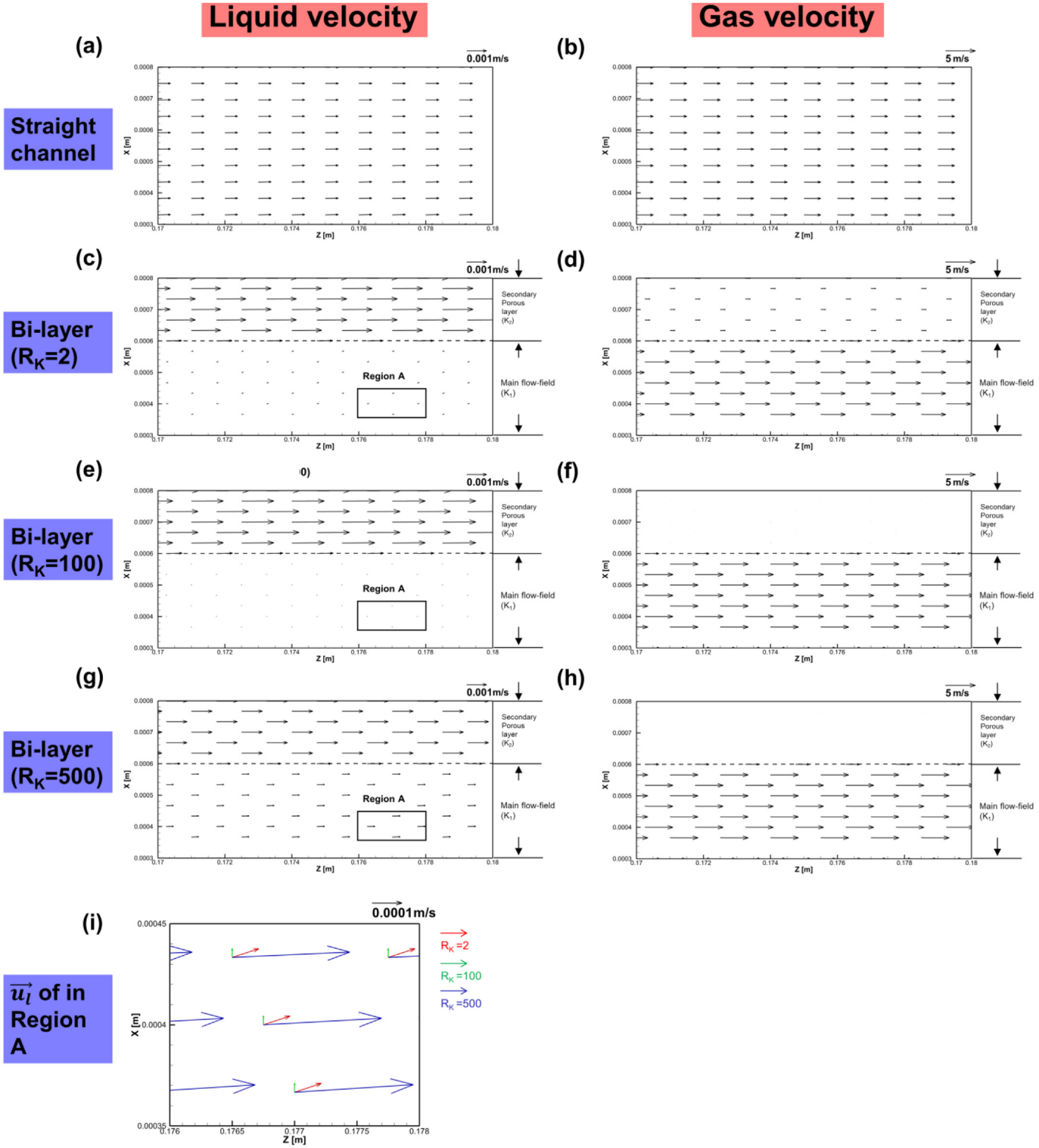

Fig. 4. Liquid and gas velocity vectors in (a, b) a straight channel, bi-porous layer flow-fields with (c, d) $R_K = 2$, (e, f) $R_K = 100$, (g, h) $R_K = 500$ near outlet region (170 mm $< z <$ 180 mm) and liquid velocity vectors in (i) region A.

studies [4]. This time-scale evaluation tells us that there is enough time ($10^{2\sim3}$sec) for secondary porous layers and main flow-fields to reach capillary equilibrium.

An order of magnitude estimation of capillary pressure difference between the two layers also supports the validity of capillary equilibrium between the two layers in through-plane (x) direction. According to Eq. (12), liquid superficial velocity in a porous medium is governed by two terms: convection term and capillary pressure gradient term, where the convection term in through-plane (x) direction is negligible owing to impermeable bi-polar plate wall at top. Therefore:

$$\rho_l u_{l,x} \sim \frac{K\lambda(1-\lambda)}{\nu}\frac{\Delta P_c}{l} \tag{19}$$

where l is a characteristic length scale (flow-field thickness), $u_{l,x}$ is a liquid velocity in through-plane (x) direction and ν is a mixture viscosity. Considering that the typical ranges of parameters are l

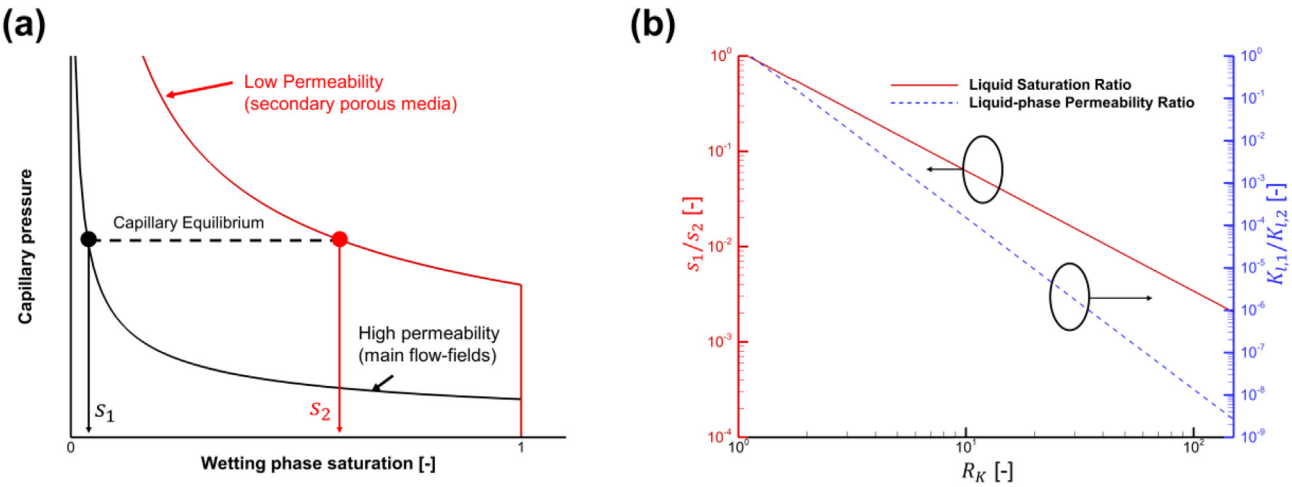

Fig. 5. (a) Schematic illustration of saturation discontinuity between two porous medium (b) Liquid saturation ratio and liquid-phase permeability ratio profile vs. permeability ratio predicted by Brook-Corey model under capillary equilibrium between two layers.

$= 0.1$–1 mm, $\nu \sim 1 \times 10^{-5}$ m^2 s^{-1}, $\lambda = 0.01$–0.5 and $u_{l,x} \sim 10^{-5\sim6} m/s$ under common PEMFC operation conditions, the characteristic capillary pressure difference (ΔP_c) is found to be on the order of 0.1 Pa. This is quite smaller than the characteristic capillary pressure of flow-fields, which is around 200 Pa according to Eq. (6). This assures capillary pressure equilibrium of bi-porous layer flow-fields in x-direction ($\Delta P_c/P_c << 1$).

Based on the discussions above, we assume that two layers are in capillary pressure equilibrium ($P_{c,1} = P_{c,2}$) for the following analytical study. Due to the permeability difference, saturation discontinuities between two layers are expected. This is schematically illustrated in Fig. 5a. Using a micro-porous layer (MPL) in a cathode electrode is a common application of using saturation discontinuity for enhancing PEMFC performance, by decreasing amount of liquid water adjacent to CL [33]. The major difference is that liquid water is wetting-phase in bi-porous layer flow-fields due to hydrophilic treatment. Therefore, low permeability medium (secondary porous media) has larger liquid saturation, unlike MPL (lower permeability medium) has lower saturation than GDL.

For further investigation of liquid saturation behavior in the two layers, capillary pressure equilibrium condition between the two layers is mathematically expressed using Brook-Corey model (Eq. (7)) as:

$$\frac{\sigma \cos\theta_1 J_c s_1^{-1/\lambda_{BC}}}{\sqrt{K_1/\varepsilon_1}} = \frac{\sigma \cos\theta_2 J_c s_2^{-1/\lambda_{BC}}}{\sqrt{K_2/\varepsilon_2}} \tag{20}$$

From **Eq.** (20), ratio of liquid saturation between two layers can be expressed as:

$$\frac{s_1}{s_2} = \left(\frac{\cos\theta_1\sqrt{\varepsilon_1}}{\cos\theta_2\sqrt{\varepsilon_2}}\right)^{\lambda_{BC}} R_K^{-\lambda_{BC}/2} \tag{21}$$

Eq. (21) is plotted in Fig. 5b *(red line)* by setting same contact angles for the both layers. According to the figure, liquid saturation of a main flow-field becomes considerably smaller with increasing permeability ratio ($s_1 \sim s_2 R_k^{-1.2}$ according to Eq. (21)), compared to the secondary porous layer. In the case of $R_K = 10$, liquid saturation of a main flow-field is around 6% of the secondary porous layer, while much smaller value of 0.3% is estimated when $R_K = 100$. This value can be further decreased if additional hydrophilic coating is applied to secondary porous layers according to Eq. (21).

The liquid water re-distribution between the two layers also affects the axial liquid velocity difference between the two layers. This is because axial liquid water velocity is strongly affected by liquid-phase permeability, which is a strong function of liquid saturation ($KK_{rk} = Ks_k^{n_k}$). According to liquid-phase momentum equation (Eq. (15)), liquid velocity is proportional to liquid-phase permeability. Assuming negligible liquid pressure gradient in x-direction, liquid velocity ratio can be approximated using Eq. (15) as:

$$\frac{u_{l,1}}{u_{l,2}} \propto \frac{K_{l,1}}{K_{l,2}} = \left(\frac{s_1}{s_2}\right)^{n_k} R_K = \left(\frac{\cos\theta_1\sqrt{\varepsilon_1}}{\cos\theta_2\sqrt{\varepsilon_2}}\right)^{n_k\lambda_{BC}} R_K^{1-n_k\lambda_{BC}/2} \tag{22}$$

The Eq. (22) shows that liquid saturation ratio plays more important role on liquid velocity ratio, compared to intrinsic permeability ratio, considering that $n_k\lambda_{BC}/2$ is usually larger than 1 ($n_k = 2$–4, $\lambda_{BC} = 2$–3). To illustrate this clearer, liquid-phase permeability ratio ($K_{l,1}/K_{l,2}^2$) versus permeability ratio is plotted in Fig. 5b *(blue line)*, by setting same contact angles for the both layers. Fig. 5b demonstrates that liquid-phase permeability ratio decreases dramatically with increasing permeability ratio (1.25×10^{-8} at $R_K = 100$). In other words, liquid flow resistance ($\propto 1/K_l$) of a main flow-field becomes significantly larger than that of the secondary layer with increasing permeability ratio. As it can be found in Eq. (22), this is mainly due to increasing relative permeability of liquid in the secondary layer.

Due to much lower liquid flow resistance in the secondary porous layer, it is expected that total liquid flow rate in a bi-porous layer flow-field is dominated by liquid flow rate in the secondary layer if permeability ratio is sufficiently large. To illustrate this quantitatively, the fraction of liquid water mass flow rate along secondary porous layers compared to total liquid water flow rate ($\dot{m}_{l,2}/\dot{m}_{l,tot}$) is derived from Eq. (22) as:

$$\left(\frac{\dot{m}_{l,2}}{\dot{m}_{l,tot}}\right)_{R_K < R_{K,th}} = \frac{R_K^{\frac{\lambda_{BC}n_k}{2}-1}\frac{A_2}{A_1}\left(\frac{\cos\theta_1}{\cos\theta_2}\sqrt{\frac{\varepsilon_1}{\varepsilon_2}}\right)^{-\lambda_{BC}n_k}}{1 + R_K^{\frac{\lambda_{BC}n_k}{2}-1}\frac{A_2}{A_1}\left(\frac{\cos\theta_1}{\cos\theta_2}\sqrt{\frac{\varepsilon_1}{\varepsilon_2}}\right)^{-\lambda_{BC}n_k}} \tag{23}$$

The Eq. (23) will be compared to 2D numerical results and discussed in detail in Section 3.2.3.

3.2.2. Flow behavior at conditions above the threshold permeability ratio

At conditions above the threshold permeability ratio, outlet region of a secondary porous layer becomes single-phase of liquid and liquid-phase permeability reaches to 1. Therefore, liquid water mass flow rate at outlet along the secondary layer is limited by intrinsic permeability ($K_l = KK_{rk} = K$). Following the similar process to the derivation of Eq. (17), the fraction of liquid water flow rate along secondary porous layers is derived and shown as:

$$\frac{\dot{m}_{l,2}}{\dot{m}_{l,tot}} = 0.8\left(\frac{\xi_{O_2}\nu_g A_2}{(1+\alpha)X_{O_2,in}\nu_l A_1}\right)/(R_K K_{rg,1}) \tag{24}$$

The only difference between the derivation of Eq. (24) and Eq. (17) is that effect of relative permeability of gas ($K_{rg,1}$) is considered in RHS of Eq. (24), since substantial amount of liquid flow is expected at outlet region of main flow-fields due to flooding inside secondary porous layers. This accounts for the increase of gas pressure drop due to presence of liquid water in main flow-fields, which is often described by a two-phase friction multiplier. Wang et al. [4] analytically derived that the two-phase friction multiplier is inverse of K_{rg} and on the order of 1 (ranges from 1 to 3 depending on operating conditions). In this work, we choose $K_{rg} = 1$ for approximation of Eq. (24) and the consequence of this approximation will be discussed in Section 3.3. Therefore:

$$\left(\frac{\dot{m}_{l,2}}{\dot{m}_{l,tot}}\right)_{R_K > R_{K,th}} \sim 0.8\left(\frac{\xi_{O_2}\nu_g A_2}{(1+\alpha)X_{O_2,in}\nu_l A_1}\right)/(R_K) \tag{25}$$

3.2.3. Fraction of liquid mass flow rate along secondary porous layers to outlets depending on permeability ratio

The main role of a bi-porous flow-field is to remove liquid water to the outlet through a secondary porous layer, instead of the main flow-field. Therefore, It is important to estimate the fraction of liquid mass flow rate along secondary porous layers to outlets, depending on permeability ratio. In previous sections, we analytically derived the fraction of liquid mass flow rate along secondary porous layers at conditions below (Eq. (23)) and above the threshold permeability ratio (Eq. (25)). These are plotted and compared to 2D simulation results in Fig. 6. It can be found from both 2D simulation and Eq. (23) that fraction of liquid flow rate through a secondary porous layer increases dramatically with increasing permeability ratio until it reaches the threshold permeability ratio. For example, this value reaches 90% even in a case of very course porous layer ($R_K = 2$). However, fraction of liquid mass flow rate through a secondary porous layer decreases with increasing permeability ratio once it is above the threshold permeability ratio, mainly due to flooding as explained previously.

Overall, analytical estimations and 2D simulations show good agreement and this supports the validity of current numerical model. However, Eq. (25) under-predicts liquid mass flow rate in a secondary porous layer above $R_{K,th}$, compared to 2D simulations. This is because relative permeability of gas is simply set to 1 in Eq. (25), and therefore the effect two-phase friction multiplier in main flow-fields is not accounted, while this is accounted in numerical model. More detailed discussion can be found in next section.

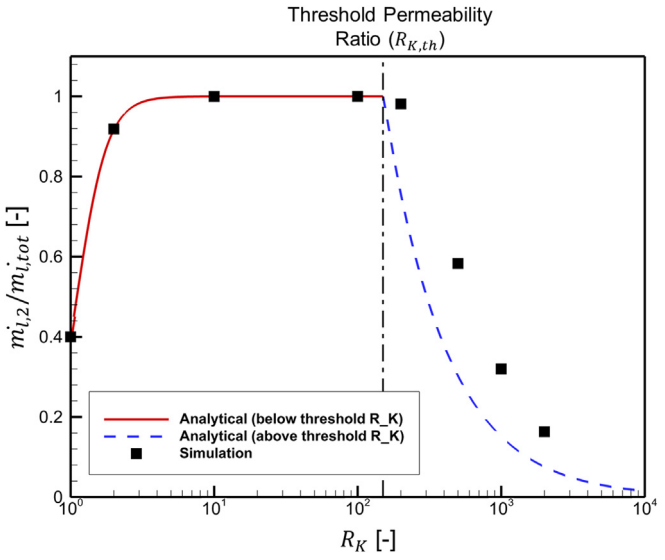

Fig. 6. Fraction of axial liquid water mass flow rate through secondary porous layer predicted by 2D simulation (*symbol*), Eq. (23) (*red solid line*) and (25) (*blue dash line*).(For interpretation of the references to colour in this figure legend, the reader is referred to the Web version of this article.)

Fig. 6 suggests that one should select the material for a secondary porous layer with a permeability ratio ranges from 10 to $R_{K,th}$, to utilize the benefits of liquid water re-distribution and avoid flooding in the secondary porous layer. However, it is risky to select the permeability ratio too close to $R_{K,th}$ since very high liquid water saturation (~0.95) is expected at outlet region, which can be seen in the case of $R_K = 100$ (Fig. 3a). Therefore, it may be desirable to select the permeability ratio ranges from 10 to $R_{K,cr}/2$ (or less). Since typical intrinsic permeability of PEMFC flow-fields is usually on the order of $10^{-8}m^2$, permeability of secondary porous layers should be higher than $10^{-10}m^2$. Note that this is much larger than a typical permeability of GDL ($\sim 10^{-11}m^2$).

Considering that permeability is proportional to square of pore diameter ($K \propto D_h^2$), ratio of pore diameter of a main flow-field to the secondary porous layer should range from 3 to 10. This is well agreed to prior experimental studies, such as PEMFCs with micro-grooved flow-fields [5–7] and bi-porous flow-fields [8]. The width of micro-grooves selected for micro-groove flow-fields is 0.2 mm while channel hydraulic diameter is 1.0 mm, according to experimental setup [5–7]. For bi-porous flow-fields by Kozakai et al. [8], it is reported that the two peaks of pore diameter distribution in porous media are reported to be 30 and 150 μm. Both flow-fields have pore diameter ratio of 5.

Note that main flow-fields are macroscopically treated as porous media in this work. However, in microscopic point of view, some liquid water can be stuck at the corner between bi-polar plate and GDL, especially if diameter of liquid droplet at this corner is much smaller than channel diameter. An experimental study with micro-grooved flow-fields by Ukata et al. [5] illustrates an effective way to circumvent this problem. In their work, slanted micro-grooves were carved in straight channels with various tilt angles to ensure that liquid water can easily move through slanted micro-grooves to upper grooves by gas shear stress [5]. It is reported that smaller tilt angle (20°) was the most effective compared to 30°, 45° [5].

3.3. Driving force for liquid water removal in secondary porous layers through outlets

The driving force that removes accumulated water in secondary porous layers through outlets is the longitudinal pressure drop imposed by gas flow through main flow-fields. Here, a schematic in Fig. 7a is shown to address the working principle. Once liquid water in a main flow-field is imbibed in the secondary porous layer, this liquid water moves along the secondary porous layer towards the outlet under its adjacent gas pressure gradient in the main flow-field, considering that $P_l = P_g - P_c$. On the other hand, the capillary effect is found to be negligibly small in the current problem considering that the gas pressure drop (3000–5000 Pa) is significantly higher than the longitudinal capillary pressure difference (~400 Pa) due to high gas velocity and very long channel (20 cm).

To understand the behavior of axial liquid water flow in secondary porous layers, axial liquid velocity, liquid-phase permeability and liquid pressure gradient along channel direction are plotted in Fig. 7b, c and d, respectively, as these three factors constitute liquid-phase momentum equation (Eq. (20)). In the cases of $R_K = 2$ and 100, liquid velocities linearly increase along channel direction due to uniform current density. Comparing with the case of $R_K = 2$, the case of $R_K = 100$ shows higher liquid velocity due to higher liquid saturation (Fig. 3b) and therefore higher liquid permeability (Fig. 7c).

It is also worth noting from Fig. 7d that magnitude of liquid pressure gradient in the case of $R_K = 100$ is smaller than the case of $R_K = 2$. This is due to higher two-phase friction multiplier owing to higher liquid saturation in the main flow-field in the case of $R_K = 2$. Overall gas pressure drop in the case of $R_K = 2$ is found to be 3971 Pa, which is 40% higher compared to that in the case of $R_K = 100$ (2863 Pa). This implies that using an optimized material for secondary porous layer can also alleviate gas pressure and voltage fluctuations, which are strongly

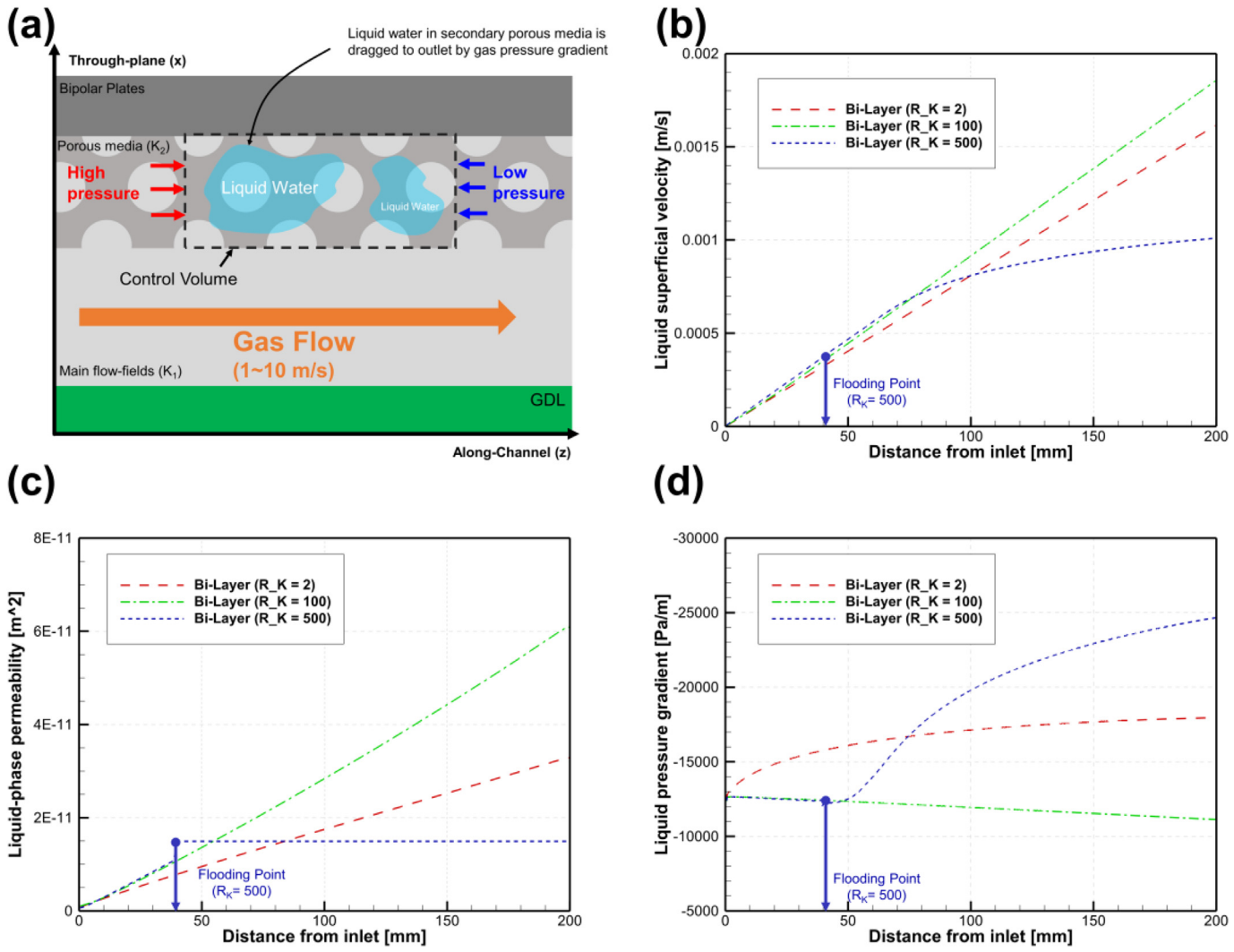

Fig. 7. (a) Schematic of liquid water transport mechanism in secondary porous layer, (b) liquid superficial velocity (c) liquid-phase permeability (d) liquid pressure gradient profile along channel direction.

influenced by presence of liquid water in flow-fields. Specifically, an experimental study by Koresawa and Utaka [6] reported that voltage fluctuations was drastically improved by using micro-grooved flow-fields.

The case of $R_K = 500$ shows smaller liquid velocity at outlet region compared to other two cases due to liquid water flooding in the secondary porous layer. The interesting point is that liquid velocity still increases beyond a flooding point. This is due to increase of gas pressure drop (overall pressure drop = 4462 Pa), owing to accumulation of liquid water in main flow-fields (see Fig. 3b). This can be seen from the increase of liquid pressure gradient in the secondary porous layer beyond flooding point (Fig. 7d). This implies that one may experience voltage and gas pressure fluctuations if a permeability ratio is above the threshold.

3.4. *Effects of liquid water re-distributions in bi-porous layer flow-fields on PEMFC performance*

Cross-sectional averaged liquid saturation profiles in GDL are first shown in Fig. 8a since liquid water build-up in GDL is unfavorable to cell performance [34]. According to Fig. 8a, liquid water saturation in GDL decreases with increasing permeability ratio until $R_{K,th}$, primary due to decreasing liquid saturation in main flow-fields (Fig. 3b). Specifically, at $R_K = 100$, the saturation curve is almost uniform since liquid saturation in the main flow-field reaches almost zero (Fig. 3b). However, liquid saturation in GDL starts to increase with increasing permeability ratio above $R_{K,th}$, from flooding points as seen in the case of $R_K = 200$ and 500. This is because liquid water in main flow-fields starts to accumulate along axial direction beyond flooding points. This increases liquid water coverage between flow-fields and GDL and hence increases liquid water saturation in GDL.

Liquid water build-up in GDL directly influences oxygen diffusion to CL. Here, oxygen mass fraction profiles at GDL/CL interface are plotted in Fig. 8b. As seen from the figure, oxygen concentration near outlet ($180\text{ mm} < z < 200\text{ mm}$) increases with increasing permeability ratio until $R_{K,th}$. Specifically, the case of $R_K = 100$ shows up to twice oxygen mass fraction compared to the straight channel case. This is primarily due to decreasing liquid saturation in GDL as seen in Fig. 8a, and hence increasing oxygen diffusivity. Once permeability ratio is over the threshold, however, oxygen concentration near outlet decreases with increasing permeability ratio due to liquid water accumulation in GDL. It implies that the flooding in secondary porous layers is especially critical to oxygen transport near outlet region, which suffers from the concentration loss the most. Therefore, permeability of a secondary porous layer should be selected carefully for optimum performance.

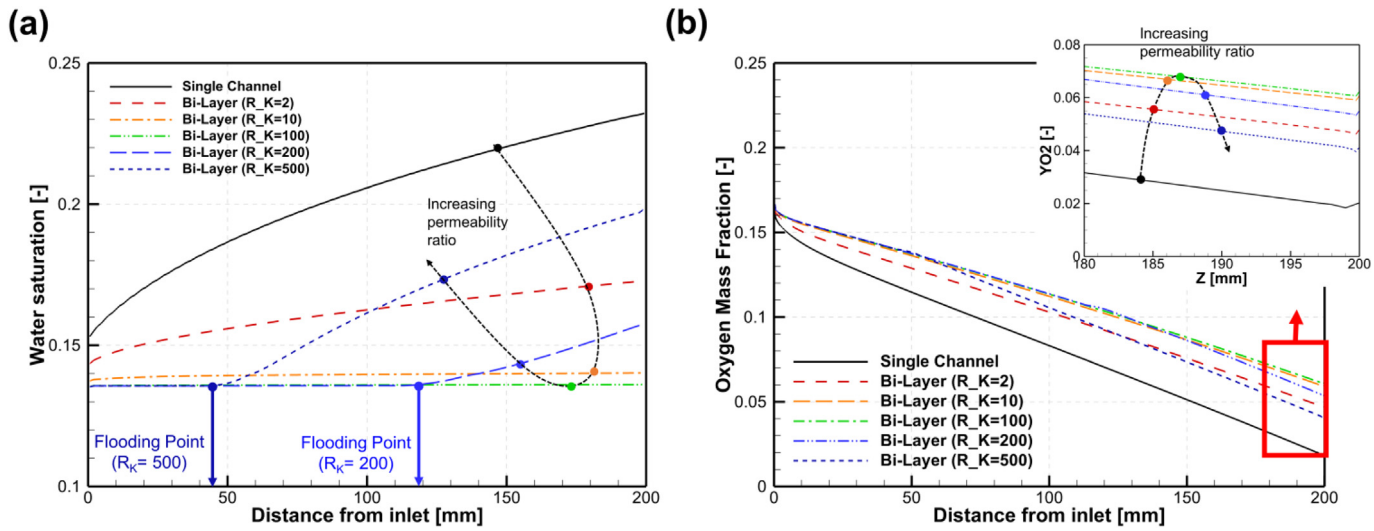

Fig. 8. (a) cross-sectional averaged liquid saturation profiles in GDL (b) oxygen mass fraction profiles at GDL/CL interface.

4. Conclusions

In this work, we develop a fundamental understanding of liquid water re-distributions in bi-porous layer flow-fields of PEMFCs by conducting numerical and analytical studies. We show that permeability ratio is the key parameter for liquid water re-distributions. It is also found that two-phase flow behavior at conditions below and above the threshold permeability ratio are fundamentally different.

At conditions below the threshold permeability ratio, liquid water re-distributions inside bi-porous flow-fields are governed by capillary equilibrium. And more liquid water can be drawn from main flow-fields by increasing permeability ratio or hydrophilicity of secondary porous layers. Positive consequences of liquid water re-distributions are found to be i) less pressure/voltage fluctuations owing to less amount of liquid water in main flow-fields, ii) less liquid water accumulation in GDL and iii) improvement in oxygen diffusion to CL.

At conditions above the threshold permeability ratio, however, secondary porous layers become fully flooded (single-phase liquid) starting from outlets and this region expands with increasing permeability ratio. This causes liquid water accumulation in main flow-fields from flooding points, which attributes negative consequences to cell performance, such as i) liquid water build-up in GDL and ii) poor oxygen diffusion to CL and iii) pressure/velocity fluctuations.

To effectively absorb liquid water from main flow-fields and avoid flooding in secondary porous layers, we suggest choosing a permeability ratio below the threshold, and ranges between 10 and $R_{K,th}/2$. We believe that the current work points out the importance of liquid water re-distributions in next-generation flow-fields for better water management of PEMFCs and will serve as a useful guidance for future fuel cell stack and flow-fields design.

Appendix. Derivation of the threshold permeability ratio in partially humidified cases

The derivation is similar to the derivation of the threshold permeability ratio in fully-humidified case. The difference lies on the expression on total liquid water flow rate. According to mass balance, total liquid water flow rate in partially humidified case can be expressed as:

$$\dot{m}_{l,out} = \dot{m}_{H_2O,gen} + \left(\dot{m}_{H_2O,g,in} - \dot{m}_{H_2O,g,out}\right) \tag{A1}$$

Axial molar flow rate of vapor is expressed as $\dot{n}_{H_2O,g} = \dot{n}_g X_{H_2O}$. Therefore, axial mass flow rate of vapor is expressed as $\dot{m}_{H_2O,g} = (MW_{H_2O}/MW_{air})X_{H_2O,g}\dot{m}_g$. Using this expression and assuming uniform axial gas flow rate, Eq. (A1) can be re-arranged as:

$$\dot{m}_{l,out} = \frac{MW_{H_2O}}{MW_{air}}\left(2\frac{(1+\alpha)X_{O_2}}{\xi_{O_2}} + \left(X_{H_2O,g,in} - X_{H_2O,g,sat}\right)\right)\dot{m}_g \tag{A2}$$

By plugging Eq. (A2) to Eq. (16), the threshold permeability ratio in partially humidified case is derived as:

$$R_{K,th} = 1.6\left(\frac{\nu_g A_2}{\nu_l A_1}\right)/\left(2\frac{(1+\alpha)X_{O_2}}{\xi_{O_2}} + \left(X_{H_2O,g,in} - X_{H_2O,g,sat}\right)\right) \tag{A3}$$

If a cathode flow-field is fully humidified, water vapor concentration at cathode inlet and outlet are equal. Therefore, Eq. (A3) reduces to Eq. (18). It can be also found that the threshold permeability ratio increases with decreasing relative humidity, according to Eq. (A3).

References

[1] F.Y. Zhang, X.G. Yang, C.Y. Wang, Liquid water removal from a polymer electrolyte fuel cell, J. Electrochem. Soc. 153 (2006) A225, https://doi.org/10.1149/1.2138675.
[2] Y. Li, C.Y. Wang, Modeling of transient platinum degradation in a low Pt-Loading PEFC under current cycling, J. Electrochem. Soc. 164 (2017) 171–179, https://doi.org/10.1149/2.0081704jes.
[3] T. Kotaka, Y. Tabuchi, U. Pasaogullari, C.Y. Wang, Electrochimica acta impact of interfacial water transport in PEMFCs on cell performance, Electrochim. Acta 146 (2014) 618–629, https://doi.org/10.1016/j.electacta.2014.08.148.
[4] Y. Wang, S. Basu, C.Y. Wang, Modeling two-phase flow in PEM fuel cell channels 179 (2008), pp. 603–617, https://doi.org/10.1016/j.jpowsour.2008.01.047.
[5] Y. Utaka, A. Okabe, Y. Omori, Proposal and examination of method of water removal from gas diffusion layer by applying slanted microgrooves inside gas channel in separator to improve polymer electrolyte fuel cell performance, J. Power Sources 279 (2015) 533–539, https://doi.org/10.1016/j.jpowsour.2015.01.050.
[6] R. Koresawa, Y. Utaka, Water control by employing microgrooves inside gas channel for performance improvement in polymer electrolyte fuel cells, Int. J.

Hydrogen Energy 40 (2015) 8172–8181, https://doi.org/10.1016/j.ijhydene.2015.04.113.
[7] Y. Utaka, R. Koresawa, Effect of wettability-distribution pattern of the gas diffusion layer with a microgrooved separator on polymer electrolyte fuel cell performance, J. Power Sources 363 (2017) 227–233, https://doi.org/10.1016/j.jpowsour.2017.07.095.
[8] M. Kozakai, K. Date, Y. Tabe, T. Chikahisa, Improving gas diffusivity with bi-porous flow-field in polymer electrolyte membrane fuel cells, Int. J. Hydrogen Energy 41 (2016) 13180–13189, https://doi.org/10.1016/j.ijhydene.2016.05.131.
[9] N. Konno, S. Mizuno, H. Nakaji, Y. Ishikawa, Development of compact and high-performance fuel cell stack, SAE Int. J. Altern. Powertrains. 4 (2015) 123–129, https://doi.org/10.4271/2015-01-1175.
[10] Y. Nonobe, Development of the Fuel Cell Vehicle Mirai, (2017), pp. 5–9, https://doi.org/10.1002/tee.22328.
[11] K. Kojima, Toyota MIRAI Fuel Cell Vehicle and Progress toward a Future Hydrogen Society, (2017), pp. 45–49.
[12] J. Kim, G. Luo, C.Y. Wang, Modeling Two-phase Flow in Three-dimensional Complex Flow-fields of Proton Exchange Membrane Fuel Cells, (2017), https://doi.org/10.1016/j.jpowsour.2017.09.003.
[13] C.Y. Wang, P. Cheng, A multiphase mixture model for multiphase, multicomponent transport in capillary porous media - I. Model development, Int. J. Heat Mass Tran. 39 (1996) 3607–3618, https://doi.org/10.1016/0017-9310(96)00036-1.
[14] C.Y. Wang, C. Beckermann, A two-phase mixture model of liquid-gas flow and heat transfer in capillary porous media-I. Formulation, Int. J. Heat Mass Tran. 36 (1993) 2747–2758, https://doi.org/10.1016/0017-9310(93)90094-M.
[15] Y. Wang, C.Y. Wang, A Nonisothermal, Two-phase Model for Polymer Electrolyte Fuel Cells, (2008), https://doi.org/10.1149/1.2193403 0–7.
[16] F.M. White, Fluid Mechanics, eighth ed., McGraw-Hill, 2015.
[17] Y. Wang, S. Basu, C.Y. Wang, Modeling two-phase flow in PEM fuel cell channels 179 (2008) 603–617, https://doi.org/10.1016/j.jpowsour.2008.01.047.
[18] S. Basu, J. Li, C.Y. Wang, Two-phase flow and maldistribution in gas channels of a polymer electrolyte fuel cell, J. Power Sources 187 (2009) 431–443, https://doi.org/10.1016/j.jpowsour.2008.11.039.
[19] W.S. Xu, P.Y. Luo, L. Sun, N. Lin, A prediction model of the capillary pressure j-function, PLoS One 11 (2016) 1–9, https://doi.org/10.1371/journal.pone.0162123.
[20] J.T. Gostick, M.W. Fowler, M.A. Ioannidis, M.D. Pritzker, Y.M. Volfkovich, A. Sakars, Capillary pressure and hydrophilic porosity in gas diffusion layers for polymer electrolyte fuel cells, J. Power Sources 156 (2006) 375–387, https://doi.org/10.1016/j.jpowsour.2005.05.086.
[21] A.J. Desbarats, Upscaling capillary pressure???Saturation curves in heterogeneous porous media, Water Resour. Res. 31 (1995) 281–288, https://doi.org/10.1029/94WR02677.
[22] C. Van Duijn, M. De Neef, Self-similar Profiles for Capillary Diffusion Driven Flow in Heterogeneous Porous media, (1996), p. 24.
[23] C.J. Van Duijn, J. Molenaar, M.J. Neef, The effect of capillary forces on immiscible two-phase flow in heterogeneous porous media, Transport Porous Media 21 (1995) 71–93, https://doi.org/10.1007/BF00615335.
[24] R.H. Brooks, a T. Corey, Hydraulic Properties of Porous media, Hydrol. Pap. Color vol. 3, State Univ. Fort Collins CO, 1964, p. 27 pgs. doi:citeulike-article-id:711012.
[25] Martinus Th Van Genuchten, A closed-form equation for predicting the hydraulic conductivity of unsaturated soils, Soil Sci. Soc. Am. J. 44 (1980), https://doi.org/10.2136/sssaj1980.03615995004400050002x.
[26] F. Liu, G. Lu, C.Y. Wang, Water transport coefficient distribution through the membrane in a polymer electrolyte fuel cell, J. Membr. Sci. 287 (2007) 126–131, https://doi.org/10.1016/j.memsci.2006.10.030.
[27] S. Basu, C.Y. Wang, K.S. Chen, Two-phase flow maldistribution and mitigation in polymer electrolyte fuel cells, J. Fuel Cell Sci. Technol. 6 (2009) 31007, https://doi.org/10.1115/1.2971124.
[28] R.B. Bird, W.E. Stewart, E.N. Lightfoot, Transport Phenomena, (1960).
[29] S.V. Patankar, Numerical Heat Transfer and Fluid Flow, Hemisphere Publishing Corp., New York, 1980.
[30] A.K. Srouji, L.J. Zheng, R. Dross, A. Turhan, M.M. Mench, Ultra-high current density water management in polymer electrolyte fuel cell with porous metallic flow field, J. Power Sources 239 (2013) 433–442, https://doi.org/10.1016/j.jpowsour.2013.03.145.
[31] Y. Wang, C.Y. Wang, Modeling polymer electrolyte fuel cells with large density and velocity changes, J. Electrochem. Soc. 152 (2005) A445, https://doi.org/10.1149/1.1851059.
[32] J. Benziger, E. Chia, E. Karnas, J. Moxley, C. Teuscher, I.G. Kevrekidis, The stirred tank reactor polymer electrolyte membrane fuel cell, AIChE J. 50 (2004) 1889–1900, https://doi.org/10.1002/aic.10158.
[33] U. Pasaogullari, C.Y. Wang, Two-phase transport and the role of micro-porous layer in polymer electrolyte fuel cells, Electrochim. Acta 49 (2004) 4359–4369, https://doi.org/10.1016/j.electacta.2004.04.027.
[34] D. Hayashi, A. Ida, S. Magome, Synchrotron x-ray visualization and simulation for operating fuel cell diffusion layers, SAE Tech. Pap. (2017), https://doi.org/10.4271/2017-01-1188.

List of symbols

A: Cross-sectional area
C_{O_2}: Molar concentration of oxygen (mol m^{-3})
CH: Flow channel, or flow-fields
D_h: Hydraulic diameter (m)
$D_{O_2}^{eff}$: Effective diffusivity of oxygen (m^2 s^{-1})
I: Current density (A cm^{-2})
$\overrightarrow{j_l}$: Mass flux of liquid (kg m^2s)
M: Molecular weight (kg mol^{-1})
mf_l^k: Mass fraction of species *k* in liquid phase
P: Pressure (Pa)
S: Source term in transport equations
s: Saturation
T: Temperature (K)
U: Characteristic velocity scale (m s^{-1})
$\overrightarrow{u}$: Mixture superficial velocity (m s^{-1})
X: Mole fraction
Y: Mass fraction

Greek

γ_c: Correction factor for species convection
ε: Porosity
μ: Dynamic viscosity (kg $m^{-1}s^{-1}$)
ν: Kinematic viscosity (m^2 s^{-1})
ρ: Density (kg m^{-3})

Superscript and subscripts

1: Main flow-field
2: Secondary porous layer
g: Gas
i: Species
k: Phase
l: Liquid
w: Wetting-phase